frontiers in Materials

ORIGINAL RESEARCH
published: 06 August 2021
doi: 10.3389/fmats.2021.739859

N-Doped Carbon Boosted the Formation of Few-Layered MoS_2 for High-Performance Lithium and Sodium Storage

Junfeng Li[1,2*†], *Xianzi Zhou*[3,4†], *Kai Lu*[4], *Chao Ma*[3,4], *Liang Li*[4], *Haibao Wang*[4], *Xuejiao Han*[4], *Hengchao Sun*[3,4] *and Shinbin Sun*[1*]

[1]College of Logistics and Engineering, Shanghai Maritime University, Shanghai, China, [2]Shanghai Key Laboratory of Magnetic Resonance, School of Physics and Electronic Science, East China Normal University, Shanghai, China, [3]Beijing Smartchip Semiconductor Technology Co., Ltd, Beijing, China, [4]Beijing Smart-Chip Microelectronics Technology Co., Ltd, Beijing, China

OPEN ACCESS

Edited by:
Xingtao Xu,
National Institute for Materials Science, Japan

Reviewed by:
Wenliang Song,
University of Shanghai for Science and Technology, China
Jian Lv,
Nanyang Technological University, Singapore

***Correspondence:**
Junfeng Li
jfli@shmtu.edu.cn
Shinbin Sun
sunshibin@shmtu.edu.cn

[†]These authors have contributed equally to this work

Specialty section:
This article was submitted to Carbon-Based Materials, a section of the journal Frontiers in Materials

Received: 12 July 2021
Accepted: 29 July 2021
Published: 06 August 2021

Citation:
Li J, Zhou X, Lu K, Ma C, Li L, Wang H, Han X, Sun H and Sun S (2021) N-Doped Carbon Boosted the Formation of Few-Layered MoS_2 for High-Performance Lithium and Sodium Storage. Front. Mater. 8:739859. doi: 10.3389/fmats.2021.739859

Molybdenum sulfide (MoS_2) has become a potential anode of lithium-ion batteries (LIBs) and sodium-ion batteries (SIBs) due to its high theoretical capacity and low cost. However, the volume expansion, poor electrical conductivity and dissolution of polysulfides in the electrolyte during the cycling process severely limited its applications. Herein, few-layered MoS_2@N-doped carbon (F-MoS_2@NC) was synthesized through a facile solvothermal and annealing process. It was found that the addition of N-doped carbon precursor could significantly promote the formation of few-layered MoS_2 and improve the performances of lithium and sodium storage. A high reversible capacity of 482.6 mA h g^{-1} at a high current density of 2000 mA g^{-1} could be obtained for LIBs. When used as anode material for SIBs, F-MoS_2@NC hybrids could maintain a reversible capacity of 171 mA h g^{-1} at a high current density of 1,000 mA g^{-1} after 600 cycles. This work should provide new insights into carbon hybrid anode materials for both LIBs and SIBs.

Keywords: N-doped carbon, molybdenum sulfide, high performance, anode, lithium-ion batteries, sodium-ion batteries

INTRODUCTION

During the last few decades, lithium-ion batteries (LIBs) have been used in almost every facets of people's daily life, such as portable electronic products, electric vehicles and medical electronics (Tarascon and Armand, 2001; Li et al., 2019a; Ni et al., 2019a; Pu et al., 2021). However, the current graphite anode couldn't meet the increasing energy demand of advanced equipments due to its low theoretical capacity and poor rate ability (Ni et al., 2019b; Li et al., 2020; Yan et al., 2020). On the other hand, sodium ion batteries (SIBs) are considered as a potential candidate of LIBs in large-scale energy storage systems due to the abundant natural reserves of sodium compared with lithium (Yabuuchi et al., 2014; Nayak et al., 2018). However, due to the mismatch between ionic radius of sodium ion and graphite interlayer ($d_{(002)}$ = 0.335 nm), the commerical graphite-type anode of LIBs show very limited capacity for SIBs (Liu and Mustarelli, 2020). Hence, it is very exigent to explore high performance anode materials of LIBs and SIBs (Palacin, 2009). In recent years, transitional metal dichalcogenides (TMDs) with the advantages of low cost and environmental begnity have been regarded as promising candidate anodes for secondary LIBs and SIBs (Peng et al., 2016; Li et al., 2021). In addition, TMDs not only possesses lower activation energy between metal and sulfur than metallic oxides, but also demonstrates much higher theoretical capacity than carbon materials. The

low activation energy is beneficial to the conversion reaction during charge/discharge process, while the high theoretical capacity of active material is vital to the energy density of both LIBs and SIBs (Yan et al., 2005; Yuan et al., 2011). Espically, molybdenum sulfide (MoS_2) with a represenative two-dimensional structure demonstrates a superior design flexibility and high theoretical capacity when applied as anode of LIBs and SIBs (Liu et al., 2018; Li et al., 2019b). However, during the cycle process, due to the volume change, dissolution of polysulfides and poor electronic conductivity, the electrode will eventually be powdered, electric contact loss, poor rate capacity and rapid capacity attenuation.

Up to now, various strategies have been developed to improve the electrochemical performance of MoS_2 anode. An effective method is to fabricate nanometer materials, which are easy to release stress. In addition, the nano-scale particle size can effectively shorten the ion diffusion distance and promote the migration of alkali metal ions during the charge and discharge process (Hu et al., 2014; Kang et al., 2017). Another widely used method is to combine with conductive matrix such as amorphous carbon (Balogun et al., 2016). The conductive matrix not only improves the electron transport capacity, but also adapts to the changing volume during the cycle. In addition, heteroatom doping can improve the properties of carbon matrix (Balogun et al., 2016). Heteroatom doping, especially N doping in carbon, can produce extrinsic conductivity, which is beneficial to the contact between carbon and MoS_2. More recently, the synthesis of MoS_2 with few-layered structure has also been drawn extensive attention due to its shorter ion pathway and higher ion diffusion mobility compared with multi-layered structure (Lv et al., 2015). Although much progress has been made so far, the rational utilization of those strategies for both lithium and sodium storage is still highly desirable.

Herein, we reported the fabrication of few-layered MoS_2@N-doped carbon (F-MoS_2@NC) nanohybrids and evaluated its application as anode of LIBs and SIBs. In this unique nanohybrid structure, the MoS_2 nanocrystals effectively promote the transfer of alkali metal ions and also shorten the alkali metal ions diffusion distance, while the N-doped carbon matrix improves the electron transport capacity, inhibits the agglomeration of nanocrystals and reduces the stress when the volume changes greatly. Furthermore, the few-layered MoS_2 structure shortens the ion channel and improves the diffusion mobility of lithium and sodium ion. In consequence, F-MoS_2@NC demonstrates a reversible capacity of 482.6 mA h g^{-1} at 2000 mA g^{-1} for LIBs and maintains a reversible capacity of 171 mA h g^{-1} at of 1,000 mA g^{-1} after 600 cycles for SIBs. The excellent lithium and sodium storage properties of F-MoS_2@NC should be derived from the synergy between N-doped carbon and few-layered MoS_2 structure.

EXPERIMENTAL

Materials

Sodium molybdate dihydrate (NMD, $Na_2MoO_4 \bullet 2H_2O$), dopamine hydrochloride (DAH, $C_8H_{12}ClNO_2$), L-cysteine ($C_3H_7NO_2S$) and ethanol are from Sinopharm and used directly.

Sample Synthesis

F-MoS_2@NC hybrids were fabricated through a facile solvothermal and annealing process. Typically, 0.3 g NMD and 0.6 g L-cysteine were added into 40 ml deionized water. Subsequently, a certain amount of DAH (0.4, 0.8 and 1.2 g) were slowly dissolved in the above solution under stirring process. The above solution was then added into 100 ml autoclave and kept at 180°C for 24 h. When the autoclave cooling to RT, the resulting samples were washed with ethanol and deionized water before drying at 60°C overnight. After then, the samples were calcinated at 800°C for 2 h with a heating rate of 2°C min^{-1} in nitrogen atmosphere to further promote crystallinity of the product. The obtaining samples prepared with different amount of DAH (0.4, 0.8 and 1.2 g) were named F-MoS_2@NC-0.4, F-MoS_2@NC-0.8 and F-MoS_2@NC-1.2, respectively. For comparison, the sample named bare MoS_2 was fabricated by the similar process without adding dopamine hydrochloride.

Characterizations

X-ray diffraction with Cu Kα radiation (XRD, λ =1.5418 Å) and thermo-gravimetric analysis with a Shimadzu-50 thermoanalyser (TGA) were used to characterize the crystal and composition of the synthesized samples. Field-emission scanning electron microscopy (FESEM, JSM-7001-F type, JEOL, Japan) and transmission electron microscopy (TEM, JEM 2010 JEOL, Japan) were used to investigate the morphology and internal structure of the samples. X-ray photoelectron spectroscopy with ESCALAB 250XI photoelectron spectrometer (XPS) was used to analyze the chemical bonds on the surface of those samples. V-Sorb 2800 P was used to study the specific surface area and porous properties of the samples, which was calculated based on the adsorption branches of the isotherms by the Barrett-Joyner-Halenda (BJH) model.

Electrochemical Measurements

The lithium and sodium storage performances of samples were studied by assembling coin type (CR 2032) in glove box filled with inert argon gas. Firstly, 70% of active material, 10% of polyvinylidene chloride and 20% of carbon black were ground in organic solvent (1-methyl-2-pyrrolidone) to obtain uniform slurry. After then, the prepared slurry was coated on the copper foil and kept at 120°C overnight in vacuum. The mass loading of the working electrode was around 1.5 mg cm^{-1}. Glass filters (Whatman) and lithium/sodium plates were used as separators and the counter electrode, respectively. For LIBs and SIBs, the electrolyte was consisted of $LiPF_6$ dissolved in dimethyl carbonate/ethylene carbonate (1 M, 1:1, w/w) and $NaClO_4$ dissolved in propylene carbonate/ethylene carbonate (1 M, 1:1, w/w), respectively. Cycling tests and cyclic voltammetry (CV) were performed within the voltage range of 0.005–3 V on a Land 2001A battery test system and electrochemical workstation (AUTOLAB PGSTA302N).

RESULTS AND DISCUSSION

The typical synthesis process of F-MoS_2@NC is demonstrated in **Figure 1**. As shown, NMD/DAH complex is first simply mixed

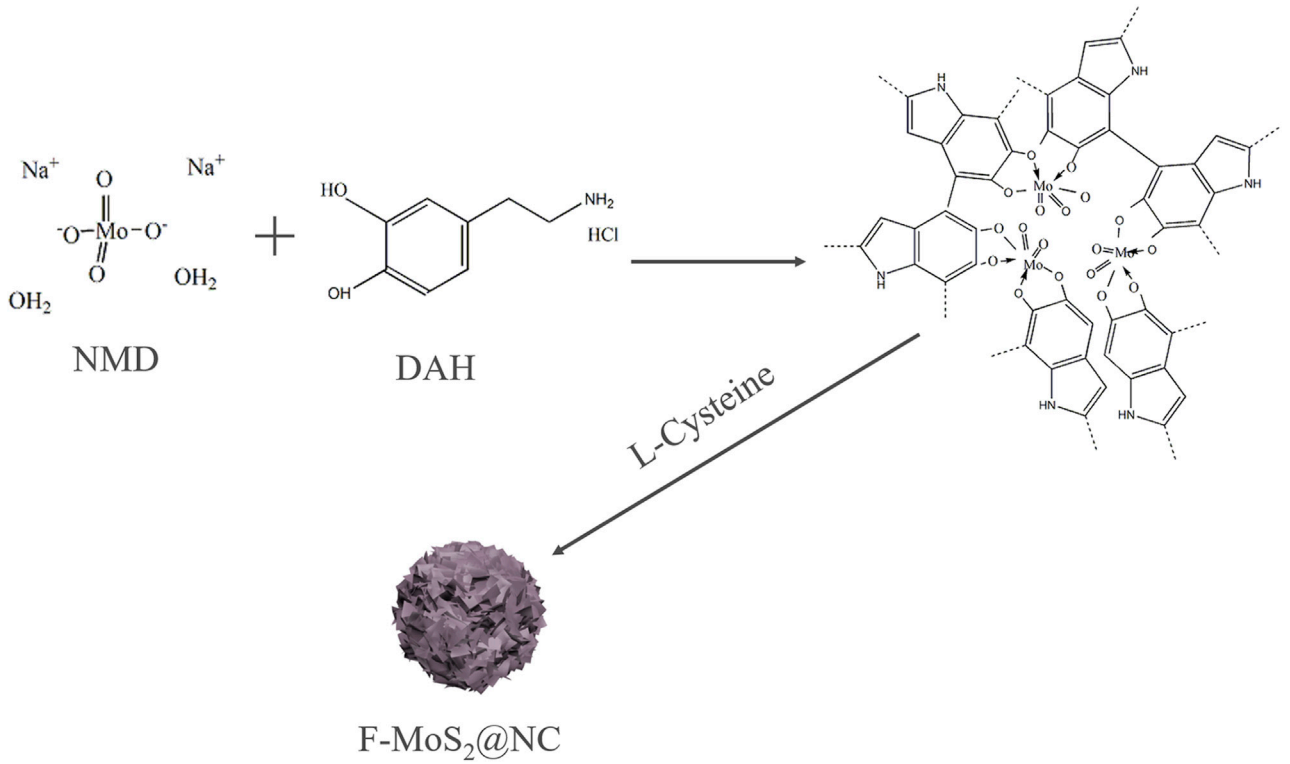

FIGURE 1 | Schematic illustration of F-MoS_2@NC fabrication process.

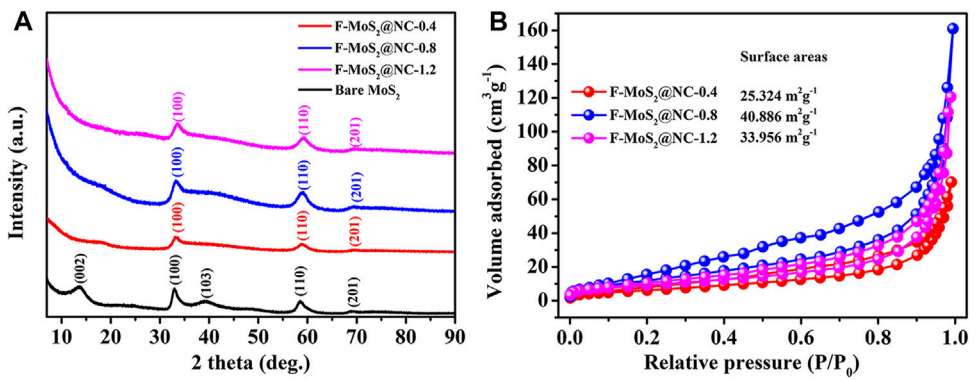

FIGURE 2 | (A) XRD patterns of bare MoS_2, F-MoS_2@NC-0.4, F-MoS_2@NC-0.8 and F-MoS_2@NC-1.2; **(B)** nitrogen adsorption-desorption curves of F-MoS_2@NC-0.4, F-MoS_2@NC-0.8 and F-MoS_2@NC-1.2.

with DAH in deionized water. Due to the chelating reaction between molybdate anion and dopamine, a uniform orange red solution is obtained. And the weak acidic environment provided by NMD inhibits the self polymerization of DAH. In the subsequent solvothermal process, DAH was partially carbonized, and L-cysteine was used as reducing agent and sulfurizing agent to promote the conversion of NMD to MoS_2. The resulting product was further calcinated at high temperature to improve the crystallinity of MoS_2 and the degree of carbonization to yield F-MoS_2@NC.

The crystalline structure of the synthesized samples was investigated by XRD, as shown in **Figure 2A**. For bare MoS_2, the diffraction peaks at 13.7°, 33.0°, 39.3°, 58.6° and 69.0° represent the (002), (100), (103), (110) and (201) of 2H MoS_2. While for F-MoS_2@NC, the diffraction peaks at 33.0°, 58.6° and 69.0° represent the (100), (110) and (201) planes of MoS_2. However, the (002) and (103) diffraction peaks of MoS_2 in the sample disappear, which should be due to the inhibition of crystal growth by the presence of carbon. Noting that the absence of (002) diffraction peak indicates the formation of few-layered MoS_2 sheets (Zhou et al., 2015; Hu

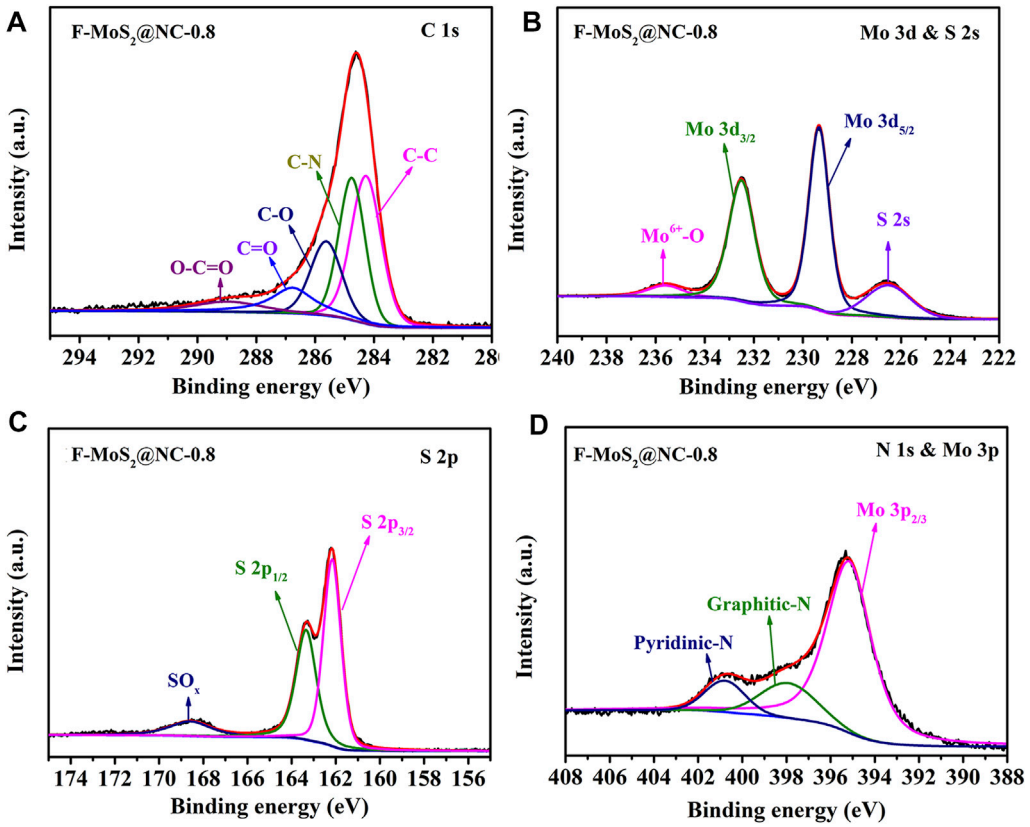

FIGURE 3 | High deconvolution of the XPS **(A)** C 1s, **(B)** Mo 3 days and S 2s, **(C)** S 2p and **(D)** N 1S and Mo 3p of F-MoS2@NC-0.8

et al., 2018; Li et al., 2021). Therefore, the addition of N-doped carbon precursor could significantly promote the formation of few-layered MoS_2 in F-MoS_2@NC. It should be noted that the diffraction peak at around 26.5° represented the (002) plane of carbon could not be observed in F-MoS_2@NC, which should be due to the low content and amorphous form of carbon. The XRD results also confirm the successful synthesis of few-layered MoS_2 structure via a facile solvothermal and annealing process. The nitrogen adsorption-desorption and porous characteristic of F-MoS_2@NC were conducted by Brunauer-Emmett-Teller method. The nitrogen adsorption-desorption curves of F-MoS_2@NC-0.4, F-MoS_2@NC-0.8 and F-MoS_2@NC-1.2 (**Figure 2B**) show a typical hysteresis loop within the P/P_0 range of about 0.3–0.9, indicating they has rich mesoporous structure (Song et al., 2019). **Supplementary Table S1** shows the pore volumes and specific surface areas of F-MoS_2@NC. It can be observed that the specific surface area of F-MoS_2@NC increased with pore volume in F-MoS_2@NC and F-MoS_2@NC-0.8 showed largest pore volume and specific surface area. For F-MoS_2@NC electrode, the large specific surface area could effectively enhance the contact between electrode/electrolyte, while the abunant pore volume will provide more ion transport pathways, which are beneficial for lithium and sodium storage (Li et al., 2013; Hou et al., 2017; Zhang et al., 2018).

XPS was used to analyze the chemical bonds on the surface of those samples, as shown in **Supplementary Figure S1** and **Figure 3**. The survey spectra of F-MoS_2@NC (**Supplementary Figure S1**) confirmed the existence of C, N, Mo, S, and O. The slight oxidation of MoS_2 in ambient environment and the existence of oxygen-containing groups resulted in the distinct oxygen signal which observed in these samples. The C1s highly deconvolution spectra of F-MoS_2@NC-0.8 (**Figure 3A**) demonstrated two fitting peaks at 284.8 and 284.3 eV, which are attributed to C-N and C-C (Li et al., 2018a; Han et al., 2019; Song et al., 2020a). Besides, the other three fitting peaks at 285.6, 286.8 and 289.0 eV can also be observed, which should be due to the existence of C–O, C=O and O–C=O in the surface of F-MoS_2@NC-0.8 (Quinlan et al., 2016; Li et al., 2018b; Ni et al., 2018; Song et al., 2019; Yue et al., 2019; Han et al., 2020), respectively. The Mo 3 d and S 2s highly deconvoluted spectra of F-MoS_2@NC-0.8 (**Figure 3B**) showed the three fitted peaks at 235.7, 232.5 and 229.4 eV are related to Mo^{6+}–O, Mo $3d_{3/2}$ and Mo $3d_{5/2}$ (Feng et al., 2015; Ahn et al., 2018; Lei et al., 2018). It should be noted that the slight surface oxidation of MoS_2 could cause the existence of Mo^{6+}–O. Besides, the S 2s peak in 226.6 eV could also clearly observed. The two fitting peaks of S $2p_{3/2}$ and S $2p_{1/2}$ could also be clearly observed at 162.2 and 163.4 eV in the highly deconvoluted S 2p spectra of F-MoS_2@NC-0.8 (**Figure 3C**). In addition, the other fitted peaks at 165.8 eV in the highly deconvoluted are ascribed to SO_x (x = 2–4) (Zhao et al., 2019; Song et al., 2020b). The fitted peaks of pyridinic-N and

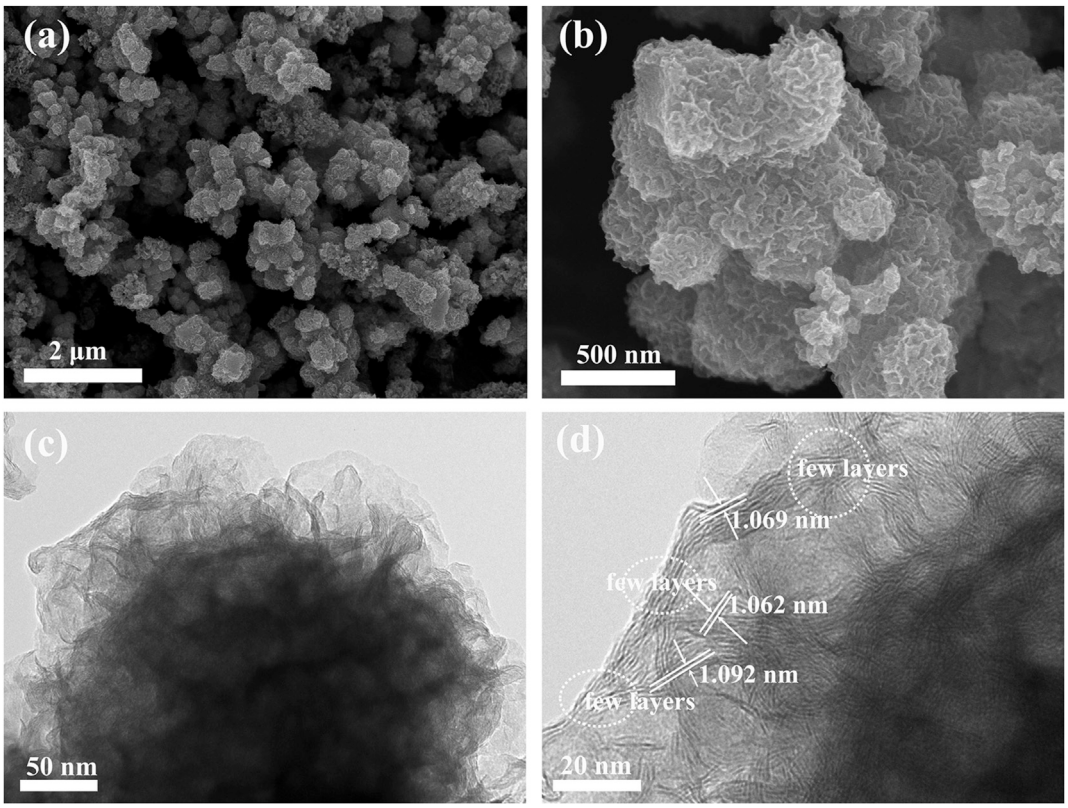

FIGURE 4 | FESEM images **(A,B)**, TEM **(C)** and high-resolution TEM **(D)** images of F-MoS_2@NC-0.8.

pyrrolic-N in the highly deconvoluted N 1S and Mo 3p spectrum of F-MoS_2@NC-0.8 (**Figure 3D**) at 398.1 and 400.8 eV could be observed, as well as the other fitted peak of Mo $3p_{2/3}$ at 395.3 eV, respectively (Ye et al., 2016; Ma et al., 2019). The high deconvolutions of C 1s, Mo 3 d and S 2s, S 2p and N 1S and Mo 3p of F-MoS_2@NC-0.4 and F-MoS_2@NC-1.2 are similar to that of F-MoS_2@NC-0.8, which are shown in **Supplementary Figure S2**. The TGA at a heating rate of 10°C min^{-1} in air was employed to characterize the weight contents of MoS_2 and carbon in F-MoS_2@NC. The TGA curves of those samples were shown in **Supplementary Figure S3**. As shown, the TGA curves demonstrated two weight loss steps that the first step below 200°C and the second step between 300 and 500°C. It should be noted that the evaporation of loss physically adsorbed water result in the first weight loss step, while the continuous combustichon of carbon and the oxidation of MoS_2 between 300 and 500°C should be contributed to the second weight loss step (Wu et al., 2018). Because carbon can burn completely in air, only MoO_3 is produced. The following equation could be used to obtain the exact content of carbon and MoS_2 can be calculated by in F-MoS_2@NC:

$$\mathrm{wt\%\,(carbon)} = 1 - \mathrm{wt\%\,(water)} - \mathrm{wt\%R} \times \mathrm{M\,(MoS_2)/M\,(MoO_3)} \quad (1)$$

$$\mathrm{wt\%\,(MoS_2)} = \mathrm{wt\%R} \times \mathrm{M\,(MoS_2)/M\,(MoO_3)} \quad (2)$$

where wt% (carbon), wt% (water) and wt% (MoS_2) represent the weight contents of carbon, water and MoS_2, M(MoS_2) and M(MoO_3) are the molecular weight of MoS_2 and MoO_3, wt%R are the residue percentages of F-MoS_2@NC after 650°C. The weight contents of MoS_2 are calculated to be 75.19, 70.09 and 64.67% in F-MoS_2@NC-0.4, F-MoS_2@NC-0.8 and F-MoS_2@NC-1.2 (See details in **Supplementary Table S1**), respectively.

Morphological and structural characteristics of F-MoS_2@NC-0.8 were studied by SEM and TEM. As exhibited in **Figures 4A,B**, the spherical product is named F-MoS_2@NC-0.8. After solvothermal treatment and annealing treatment, ~300 nm spheres with rough surface can be obtained. The surface morphologies of F-MoS_2@NC-0.4 and F-MoS_2@NC-1.2 are similar to that of F-MoS_2@NC-0.8, as shown in **Supplementary Figure S4**. Besides, the uniformly distributed elements of Mo, S and C in F-MoS_2@NC-0.8 were confirmed by the EDS mapping measurement (**Supplementary Figure S5**). The element of N could not be detected due to its low weight percentage. The SEM and TEM images of F-MoS_2@NC-0.8 (**Figures 4B,C**) indicate the microspheres consisting of ultrathin crumpled nanosheets. High resolution TEM image displays F-MoS_2@NC-0.8 (**Figure 4D**), in which several layers of MoS_2 nanosheets with an enlarged interlayer distance of 1.0 ~ 1.1 nm (vs. 0.62 nm for pristine MoS_2) can be observed. The expanded few-layered MoS_2 nanosheets effectively promote the

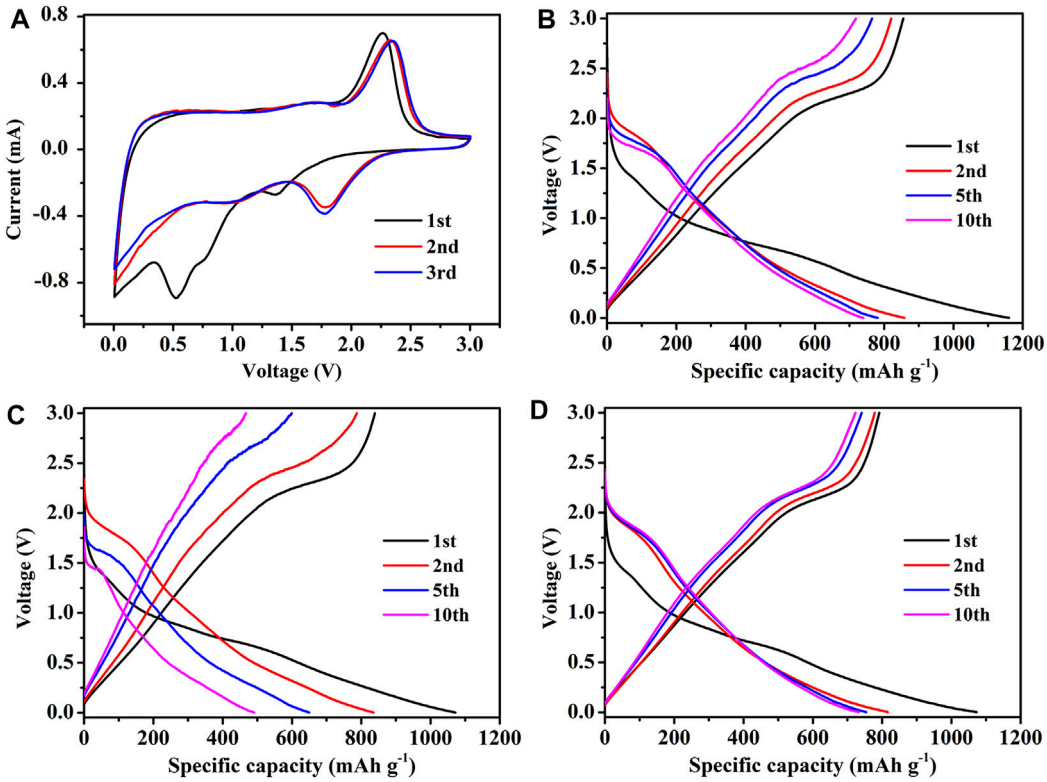

FIGURE 5 | Electrochemical performance of F-MoS_2@NC as anode of LIBs: **(A)** CV curves of F-MoS_2@NC-0.8 electrode at a scan rate of 0.2 mV s^{-1}. Charge/discharge profiles of **(B)** F-MoS_2@NC-0.8 electrode, **(C)** F-MoS_2@NC-0.4 electrode and **(D)** F-MoS_2@NC-1.2 electrode at 100 mA g^{-1}.

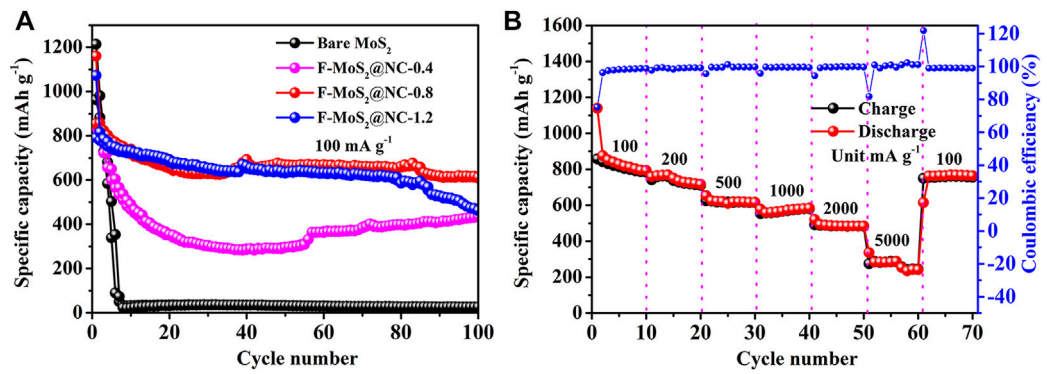

FIGURE 6 | Electrochemical performance of F-MoS_2@NC as anode of LIBs: **(A)** Cycle performances of bare MoS_2, F-MoS_2@NC-0.4, F-MoS_2@NC-0.8 and F-MoS_2@NC-1.2 at a current density of 100 mA g^{-1}. **(B)** Rate performance of F-MoS_2@NC-0.8 electrode.

transport of electrolyte and ions during charge/discharge process, thus improving the rate performance (Hu et al., 2018). It should be noted that the quantitative data of ion diffusion mobility caused by the few-layered structure was hardly obtained due to the influence of other factors, such as specific surface area and pore structure.

CR 2032 half cells were assembled using F-MoS_2@NC as the counter electrode and characterized to investigate its lithium storage performances. The initial three CV curves of F-MoS_2@NC at a sweep rate of 0.2 mV s^{-1} in the potential window of 0.005–3 V versus Li/Li^+ were displayed in **Figure 5A**. The two peaks of CV curves at 1.38 and 0.76 V in the first scan were related to the decomposition of MoS_2 into Mo and Li_2S and the intercalation of Li^+ in MoS_2, which indicates the transformation of matter from 2H MoS_2 to 1 T Li_xMoS_2, respectively (Wan et al., 2014). However, these cathodic peaks disappear after the first cycle, which indicates the nonreversible conversion reaction. The peak value located at 0.53 V in the first

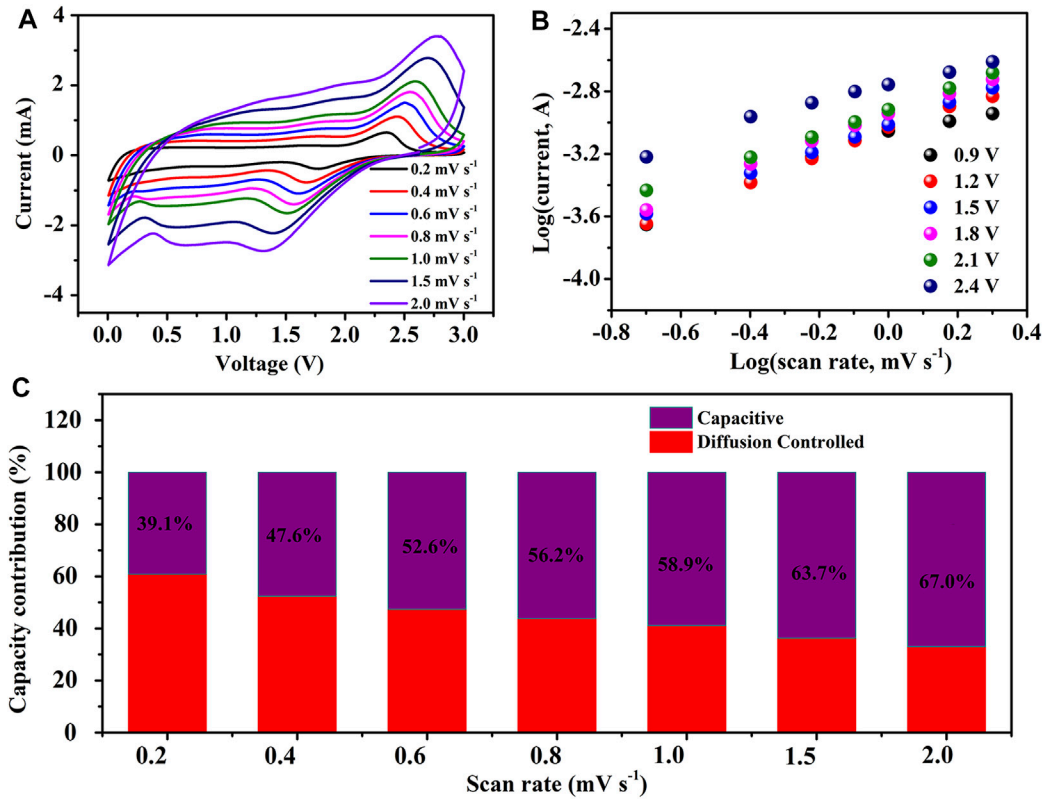

FIGURE 7 | Electrochemical behaviors of F-MoS_2@NC as anode of LIBs: **(A)** CV curves of F-MoS_2@NC-0.8 electrode at different sweep rates. **(B)** Linear relationship between log(*i*) and log(*v*) of F-MoS_2@NC-0.8 electrode at different voltage. **(C)** Ratios of capacitive and diffusion controlled contributions at different sweep rates.

cathode scan should result from the formation of solid electrolyte interface (SEI) film (Chen et al., 2016). The broad peak located at 1.65 V in the first anodic scan is related to the removal of lithium from the residual lithium intercalation layer (Li_xMoS_2). Besides, the oxidation of Li_2S to S result in another obvious peak at 2.26 V (Zhuang et al., 2015). In the subsequent scanning process, a pair of redox peaks of about 1.76/2.34 V were related to the conversion reaction between Li_2S and S, respectively (Sen et al., 2014). After the second cycle, the cathode/anode peaks are almost kept at the same position, which indicates that it has good electrochemical reversibility. The dicharge/charge profiles of F-MoS_2@NC-0.8 electrode at different cycles were demonstrated in **Figure 5B**. As shown, the initial discharge/charge specific capacities are 1,160 and 855.1 mA h g^{-1}, respectively. And the coulombic efficiency is about 73.71%. The initial large capacity loss should be attributed to the formation of SEI film in the first cycle (Cao et al., 2013). In the second cycle, the coulombic efficiency is over 95%, which indicates that the SEI film is stable. In addition, the dicharge/charge profiles of F-MoS_2@NC-0.4 and F-MoS_2@NC-1.2 electrode at different cycles are also shown in **Figures 8C,D**. It can be observed that the F-MoS_2@NC-0.4 and F-MoS_2@NC-1.2 electrode exhibit lower discharge and charge specific capacities than F-MoS_2@NC-0.8 after several cycles. Especially, the F-MoS_2@NC-0.4 electrode dropped rapidly during the cycle process, and indistinct plateau was observed in the 10th cycle, indicating that the F-MoS_2@NC-0.4 electrode had been crushed.

The galvanostatic cycling performances of bare MoS_2, F-MoS_2@NC-0.4, F-MoS_2@NC-0.8 and F-MoS_2@NC-1.2 are shown in **Figure 6**. The poor cycle performance of bare MoS_2 can be observed in **Figure 6** and the reversible capacity decreases rapidly during the cycle process. Even though the bare MoS_2 exhibits inferior cycling stability compared to some porous material, such as metal oxides and amorphous carbon, it possesses lower activation energy and high theoretical capacity and the inferior cycling stability of bare MoS_2 could be improved by the specific strategy employed in this work. When MoS_2 and N-doped carbon are combined together, compared to bare MoS_2, the F-MoS_2@NC hybrid exhibits improved cycle performance. And the cycle performances of F-MoS_2@NC are related to the proportion of N-doped carbon. With the increase of N-doped carbon content, the cycle performance is improved. However, with the further increase of N-doped carbon content, the cycle performance decreases slightly. The optimal value of N-doped carbon is 27.81%. The F-MoS_2@NC-0.8 electrode exhibited a highest reversible capacity of 608.6 mA h g^{-1} at 100 mA g^{-1}after 100 cycles. The higher capacity of F-MoS_2@NC-0.8 than

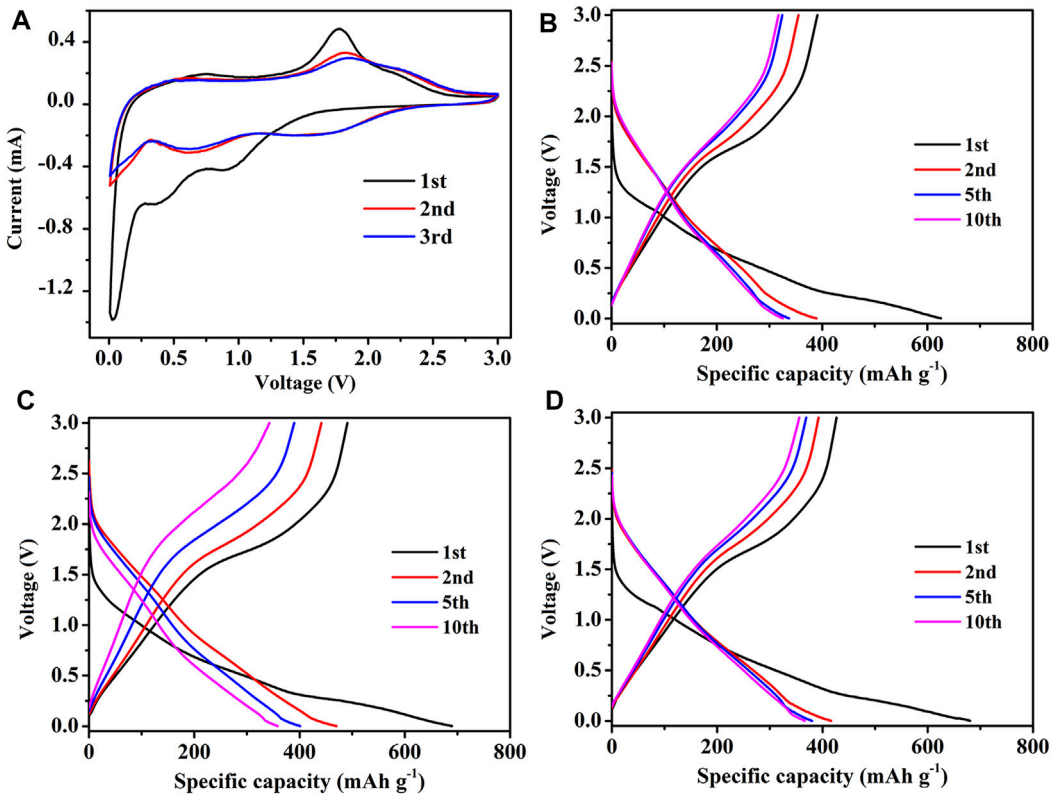

FIGURE 8 | Electrochemical performance of F-MoS_2@NC as anode of SIBs: **(A)** CV curves of F-MoS_2@NC-0.8 electrode at a scan rate of 0.2 mV s^{-1}. Charge/discharge profiles of **(B)** F-MoS_2@NC-0.8 electrode, **(C)** F-MoS_2@NC-0.4 electrode and **(D)** F-MoS_2@NC-1.2 electrode at 50 mA g^{-1}.

F-MoS_2@NC-0.4 and F-MoS_2@NC-1.2 should be due to the suitable carbon content, larger specific surface area and more mesoporous, the enhanced contact between electrode/electrolyte, as well as the transport path of lithium ion can be reduced. **Figure 6B** displays the rate performance of F-MoS_2@NC-0.8. As shown, the F-MoS_2@NC-0.8 electrode was tested at the current densities of 100, 200, 500, 1,000, 2000 and 5,000 mA g^{-1}, which displayed high reversible capacities of 814.5, 738.3, 617.6, 566.0, 482.6 and 287.4 mA h g^{-1}, respectively. It should be noted that a high reversible capacity of 758.3 mA h g^{-1} can be obtained even when the current density is restored to 100 mA g^{-1}, which indicates its excellent rate performance.

CV measurements at a series of scan rates from 0.2 to 2 mV s^{-1} were performed to explore the electrochemical kinetics of F-MoS_2@NC-0.8 electrode and the possible reasons for its excellent rate performance, as shown in **Figure 7A**. It can be observed that the shape of CV curves at different scan rates are similar. In addition, with the increase of the scanning rate, the current intensity in CV curves increases continually. In general, several mechanisms are involed in this electrochemical behavior during cycling process. The following equation can be used to analyzed the total charge stored behavior based on the CV data at different scan rates (Jiang and Liu 2019):

$$i = av^b \quad (3)$$

$$\mathrm{Log}(i) = b\log(v) + \log(a) \quad (4)$$

In those equation, i and v represents the measured current density and the scan rate, while a and b are constants, respectively. It should be noted that a value of b of 0.5 indicates the charge storage mechanism of complete diffusion control and a value of b of 1 indicates that the charge storage process of capacitance behavior dominates. The curves obtained by plotting log i versus log v are used to calculate the b value (**Figure 7B**). In fact, the slope of the curves represents the b value. When the potentials are 0.9, 1.2, 1.5, 1.8, 2.1 and 2.4 V, the b values are 0.72, 0.83, 0.8, 0.83, 0.75 and 0.59, respectively. In addition, the ratio of capacitance contribution to diffusion control contribution is calculated based on the equation:

$$i = k_2v^{1/2} + k_1v$$

In this equation, k_1 and k_2 are constants, which can be obtained by the modified equation $i_{(v)}/v^{1/2} = k_1v^{1/2} + k_2$. While $i_{(v)}$ and v represents the current density at a fixed potential and the scan rate, respectively. According to the above analysis, the ratio of capacitance contribution and diffusion control at different scan rates were calculated, as shown in **Figure 7C**. With the increasement of scan rate from 0.2 to 2 mV, the capacitance contribution also increases from 39.1% to 67.0%. It is worth noting that the high ratio of capacitance contribution is beneficial for its superior rate performance due to the improved lithium-ion diffusion and rapid electron transfer in pseudocapacitive process compared with diffusion controlled process.

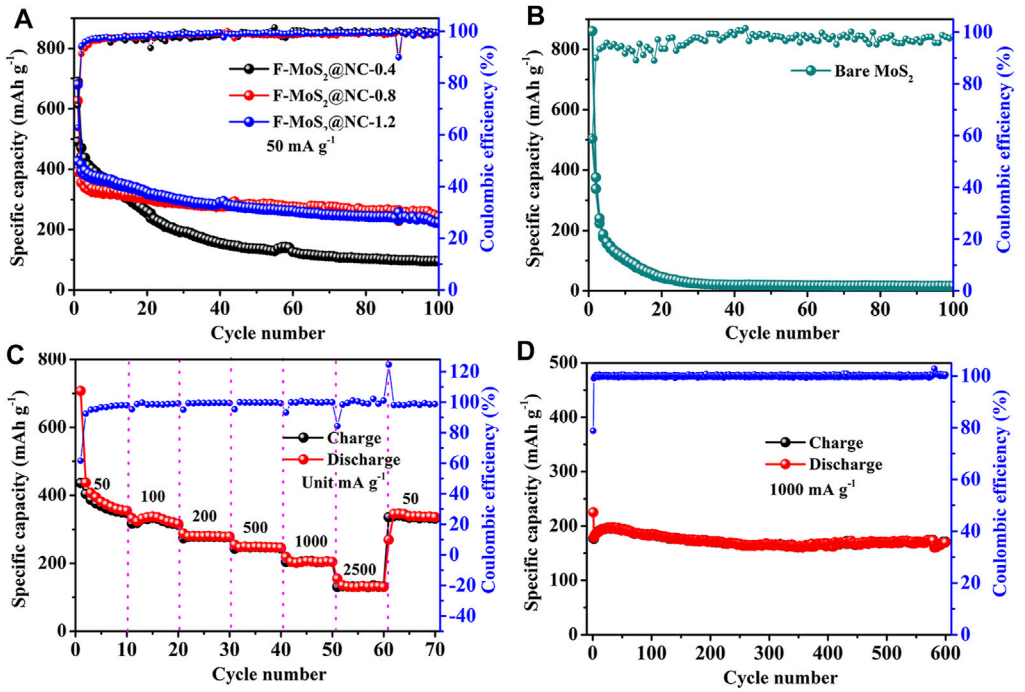

FIGURE 9 | Electrochemical performance of F-MoS_2@NC as anode of SIBs: **(A)** Cycle performances of F-MoS_2@NC-0.4, F-MoS_2@NC-0.8, F-MoS_2@NC-1.2 and **(B)** bare MoS_2 at a current density of 50 mA g^{-1}. **(C)** Rate performance of F-MoS_2@NC-0.8 electrode. **(D)** Long cycling life of F-MoS_2@NC-0.8 electrode at 1,000 mA g^{-1}.

Since the much larger size of sodium ions than lithium ions, the high-performance anode of LIBs often demonstrate poor sodium-ion storage performance when applied as anode of SIBs. Increasingly, the as-prepared F-MoS_2@NC based on the strong combination of MoS_2 and N-doped carbon shows excellent sodium storage performance. As shown in **Figure 8A**, the initial three CV curves were employed to analyze the redox behaviors of F-MoS_2@NC-0.8 for SIBs. The CV measurements were performed at a scan rate of 0.2 mV s^{-1} in the potential range of 0.005–3 V. Similar to that of LIBs, the two peaks of CV curves in the first scan at 0.91 and 0.03 V were related to the decomposition of MoS_2 into Mo and Na_2S and the intercalation of Na^+ in MoS_2, which indicates the transformation of matter from 2H MoS_2 to 1 T Na_xMoS_2, respectively (Wang et al., 2014; Wang et al., 2015). However, these cathodic peaks disappear after ths first cycle, which indicates the irreversibility of the conversion reaction. In addition, the peak located at 0.42 V in the first cathode scan should be due to the formation of SEI film on the surface of F-MoS_2@NC (Yan et al., 2015). For the first anodic scan, the oxidation of Na_2S and the formation of polysulfides caused the obvious peak of CV curves at 1.75 V (Li et al., 2018c). In the second scan, the new peaks are at 1.6 and 0.65 V, which should be realted with the formation of Na_2S and the sodium storage of Mo atoms, respectively (David et al., 2014). After the second cycle, the cathode/anode peaks are almost kept at the same position, which indicates that it has good electrochemical reversibility. **Figure 8B** shows the dicharge/charge profiles of F-MoS_2@NC-0.8 electrode at different cycles. It can be observed that the initial discharge/charge specific capacities are 391.0 and 626.2 mA h g^{-1}, and the coulombic efficiency is about 62.44%. The large capacity loss should be attributed to the SEI formation during the first cycle, similar to that of LIBs. In the subsequent cycle, the coulombic quickly reaches over 90%, which indicates the high stability of SEI film. In addition, the dicharge/charge profiles of F-MoS_2@NC-0.4 and F-MoS_2@NC-1.2 electrode at different cycles are also shown in **Figures 5C,D**. It can be observed that the F-MoS_2@NC-0.4 and F-MoS_2@NC-1.2 electrode exhibit lower discharge and charge specific capacities than F-MoS_2@NC-0.8 after several cycles. Especially, the F-MoS_2@NC-0.4 electrode dropped rapidly during the cycle, indicating that the F-MoS_2@NC-0.4 electrode was crushed. In addition, the specific discharge/charge profiles of F-MoS_2@NC electrode as anode of LIBs at 20th, 30th, 40th, 50th, 60th, 70th, 80th, 90th, and 100th cycle were also shown in **Supplementary Figure S6**. For F-MoS_2@NC-0.4 electrode, the discharge/charge platform was almost completely disappeared in those cycles, while for F-MoS_2@NC-0.8 and F-MoS_2@NC-1.2 electrodes, the discharge/charge platform could still be observed even at 100th cycle. The more distinct discharge/charge platform of F-MoS_2@NC-0.8 and F-MoS_2@NC-1.2 electrodes than F-MoS_2@NC-0.4 should be due to their higher structural stability during cycling process.

The galvanostatic cycling performances of F-MoS_2@NC-0.4, F-MoS_2@NC-0.8, F-MoS_2@NC-1.2 and bare MoS_2 as anode of SIBs are shown in **Figures 9A,B**. Similar to the LIBs presented above, the F-MoS_2@NC-0.8 electrode exhibited a highest

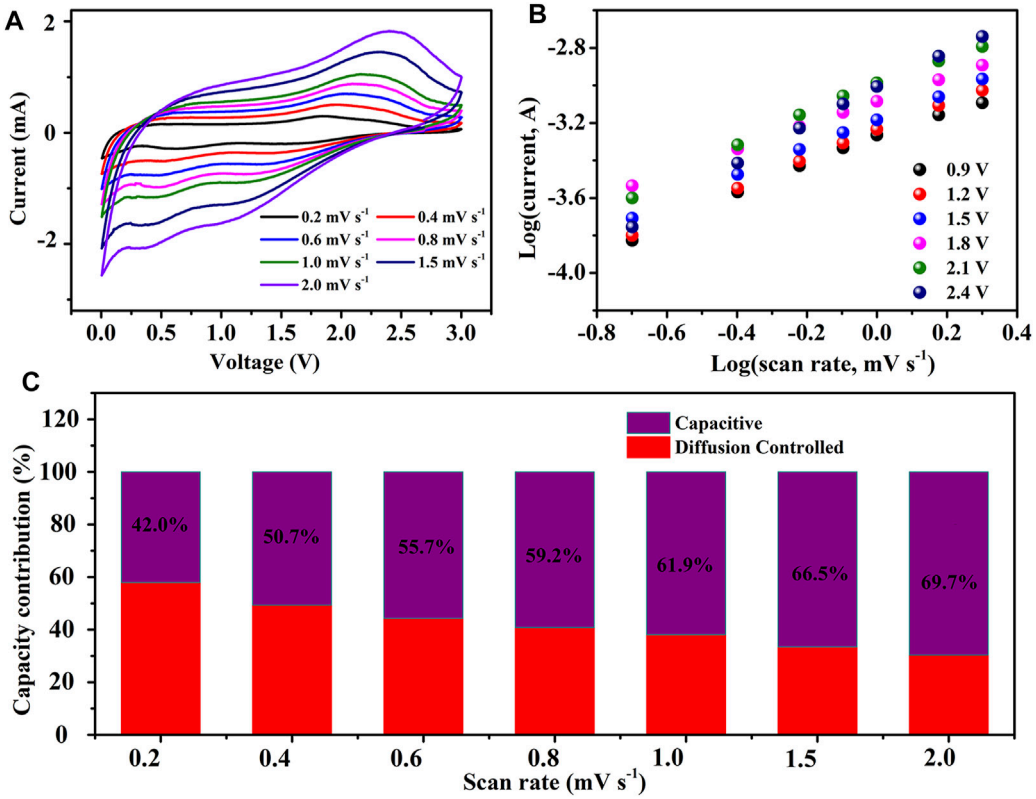

FIGURE 10 | Electrochemical behaviors of F-MoS_2@NC as anode of SIBs: **(A)** CV curves of F-MoS_2@NC-0.8 electrode at different sweep rates. **(B)** Linear relationship between log(*i*) and log(*v*) of F-MoS_2@NC-0.8 electrode at different voltage. **(C)** Ratios of pseudocapacitive and diffusion controlled contributions at different sweep rates.

reversible capacity of 241.7 mA h g^{-1} after 100 cycles at 50 mA g^{-1}, while the F-MoS_2@NC-0.4, F-MoS_2@NC-1.2 electrode and bare MoS_2 deliver lower reversible capacities of 95.3, 222.0 and 16.2 mA h g^{-1}, respectively. The best sodium storage performance of F-MoS_2@NC-0.8 in these electrodes should be related to its suitable content of carbon, larger specific area and more abundant mesoporous. In addition, the morphologies of F-MoS_2@NC-0.8 electrode after process were also investigated by SEM. As shown in **Supplementary Figure S7**, the F-MoS_2@NC-0.8 electrode could still maintain spherical structure after cycling process, indicating its structure stability. The rate performance of F-MoS_2@NC-0.8 was also shown in **Figure 9C**. As shown, the F-MoS_2@NC-0.8 electrode exhibits reversible capacities of 368.4, 333.3, 278.2, 248.2, 206.6 and 131.2 mA h g^{-1} at 50, 100, 250, 500, 1,000 and 2,500 mA g^{-1}. In addition, when the current density is restored to 50 mA g^{-1}, a high reversible capacity of 333.7 mAh g^{-1} could be obtained. Those results indicated its excellent rate performance. The long cycle performance of the electrode is of great significance to the practical application of SIBs. As shown in **Figure 9D**, the F-MoS_2@NC-0.8 electrode under the high current density of 1,000 mA g^{-1}, the electrode can still output 171.0 mA h g^{-1} after 600 cycles, and the coulomb coefficient is close to 100%, which indicates that the electrode has good structural stability and long-term cycle stability in the process of rapid charge discharge.

The electrochemical reaction kinetics of F-MoS_2@NC-0.8 as anode of SIBs was also studied. CV measurements at a series of scan rates from 0.2 to 2 mV s^{-1} were performed, which are shown in **Figure 10A**. With the increase of scanning rate, the cathode peak and anode peak become wider and the current increases. Similar to that of LIBs, the curves obtained by plotting log *i* versus log *v* are used to calculate the b value. When the potentials are 0.9, 1.2, 1.5, 1.8, 2.1 and 2.4 V, the b values are 0.74, 0.78, 0.74, 0.64, 0.8 and 1.00 (**Figure 10B**). According to the **Eq. 3**, the ratio of capacitance contribution to diffusion control contribution is calculated. As shown in **Figure 10C**, the ratio of capacitive contributions are 42.0, 50.7, 55.7, 59.2, 62.9, 66.5 and 69.7% at 0.2, 0.4, 0.6, 0.8, 1.0, 1.5 and 2.0 mV s^{-1}. The results show that with the increasement of scan rates, the rate of capacitance contribution increases continually, which will enhance the rate capability and long period stability of the system due to the improved ion diffusion and rapid electron transfer in pseudocapacitive process.

The excellent lithium and sodium storage performances of F-MoS_2@NC should be due to few-layered structure of MoS_2 and its reasonable hybridization with N-doped carbon matrix, which makes the hybrid materials have good performance as anode materials for LIBs and SIBs. Firstly, the strong combination of

N-doped carbon and ultra-small MoS_2 nanocrystals could improve the conductivity of hybrid materials, enhance the electrochemical reaction kinetics during cycling and reduce the stress caused by volume change. Secondly, the few-layered MoS_2 structure also shortens the ion channel and improves the ion diffusion mobility. Finally, because of the large specific surface area, abundant mesoporous structure and capacitance controlled electrochemical behavior, the hybrid F-MoS_2@NC materials demonstrates excellent electrochemical behavior for both lithium and sodium storage properties.

CONCLUSION

In summary, F-MoS_2@NC hybrids were synthesized through a facile solvothermal and annealing process. The XRD, SEM and TEM results confirm its few-layered MoS_2 structure, while the XPS measurement shows the existence of N-doped carbon. In fact, the existence of N-doped carbon could not only boost the formation of few-layered MoS_2 structure, but also effectively its lithium and sodium storage performance. Firstly, the few-layered MoS_2 structure could shorten the ion pathway and improve the ion diffusion mobility compared with multi-layered structure. Secondly, the N-doped carbon emhances the electron transport capacity, inhibits the agglomeration of nanocrystals and reduces the stress of MoS_2 during charge/discharge process. In addition, the relative large specific surface area and abundant also enhance the contact between electrode/electrolyte, while the abunant pore volume will provide more ion transport pathways. In consequence, a high reversible capacity of 482.6 mA h g^{-1} at a 2000 mA g^{-1} could be obtained for LIBs. As for SIBs, F-MoS_2@NC hybrids could also maintain a reversible capacity of 171 mA h g^{-1} after 600 cycles at 1,000 mA g^{-1}. The F-MoS_2@NC hybrids should be full of potential anode for both LIBs and SIBs.

DATA AVAILABILITY STATEMENT

The original contributions presented in the study are included in the article/**Supplementary Material**, further inquiries can be directed to the corresponding authors.

AUTHOR CONTRIBUTIONS

JL: Conceptualization, Methodology, Formal analysis, Writing—original draft preparation. XZ: Visualization, Data curation, Writing—original draft preparation. KL: Data curation. CM: Validation. LL, HW, XH, and HS: Writing—review and editing. SS: Resources, Supervision. All authors have read and agreed to the published version of the manuscript.

FUNDING

This research was funded by International Science and Technology Cooperation Program, grant number CU03-29, "Shuguang" Program of Shanghai Education Commission, Grant number 19SG46, Beijing Smartchip Semiconductor Technology Co., Ltd. and Beijing Smart-Chip Microelectronics Technology Co., Ltd.

SUPPLEMENTARY MATERIAL

The Supplementary Material for this article can be found online at: https://www.frontiersin.org/articles/10.3389/fmats.2021.739859/full#supplementary-material

REFERENCES

Ahn, E., Min, T., Lee, J., Lee, I., Kim, Y., and Jeen, H. (2018). Role of Surface Oxidation for Thickness-Driven Insulator-To-Metal Transition in Epitaxial MoO2 Films. *Appl. Surf. Sci.* 459, 92–97. doi:10.1016/j.apsusc.2018.07.188

Balogun, M.-S., Luo, Y., Qiu, W., Liu, P., and Tong, Y. (2016). A Review of Carbon Materials and Their Composites with alloy Metals for Sodium Ion Battery Anodes. *Carbon* 98, 162–178. doi:10.1016/j.carbon.2015.09.091

Cao, X., Shi, Y., Shi, W., Rui, X., Yan, Q., Kong, J., et al. (2013). Preparation of MoS2-Coated Three-Dimensional Graphene Networks for High-Performance Anode Material in Lithium-Ion Batteries. *Small* 9, 3433–3438. doi:10.1002/smll.201202697

Chen, G., Wang, S., Yi, R., Tan, L., Li, H., Zhou, M., et al. (2016). Facile Synthesis of Hierarchical MoS2-Carbon Microspheres as a Robust Anode for Lithium Ion Batteries. *J. Mater. Chem. A.* 4, 9653–9660. doi:10.1039/c6ta03310e

David, L., Bhandavat, R., and Singh, G. (2014). MoS2/Graphene Composite Paper for Sodium-Ion Battery Electrodes. *ACS Nano* 8, 1759–1770. doi:10.1021/nn406156b

Feng, G., Wei, A., Zhao, Y., and Liu, J. (2015). Synthesis of Flower-like MoS2 Nanosheets Microspheres by Hydrothermal Method. *J. Mater. Sci. Mater. Electron.* 26, 8160–8166. doi:10.1007/s10854-015-3476-3

Han, L., Huang, H., Fu, X., Li, J., Yang, Z., Liu, X., et al. (2020). A Flexible, High-Voltage and Safe Zwitterionic Natural Polymer Hydrogel Electrolyte for High-Energy-Density Zinc-Ion Hybrid Supercapacitor. *Chem. Eng. J.* 392, 123733. doi:10.1016/j.cej.2019.123733

Han, Y., Shi, L., Luo, X., Chen, X., Yang, W., Tang, W., et al. (2019). A Signal-On Fluorescent Sensor for Ultra-trace Detection of Hg2+ via Ag+ Mediated Sulfhydryl Functionalized Carbon Dots. *Carbon* 149, 355–363. doi:10.1016/j.carbon.2019.04.052

Hou, H., Shao, L., Zhang, Y., Zou, G., Chen, J., and Ji, X. (2017). Large-Area Carbon Nanosheets Doped with Phosphorus: A High-Performance Anode Material for Sodium-Ion Batteries. *Adv. Sci.* 4, 1600243. doi:10.1002/advs.201600243

Hu, X., Li, Y., Zeng, G., Jia, J., Zhan, H., and Wen, Z. (2018). Three-Dimensional Network Architecture with Hybrid Nanocarbon Composites Supporting Few-Layer MoS2 for Lithium and Sodium Storage. *ACS Nano* 12, 1592–1602. doi:10.1021/acsnano.7b08161

Hu, Z., Wang, L., Zhang, K., Wang, J., Cheng, F., Tao, Z., et al. (2014). MoS2Nanoflowers with Expanded Interlayers as High-Performance Anodes for Sodium-Ion Batteries. *Angew. Chem. Int. Ed.* 53, 12794–12798. doi:10.1002/anie.201407898

Jiang, Y., and Liu, J. (2019). Definitions of Pseudocapacitive Materials: a Brief Review. *Energy Environ. Mater.* 2, 30–37. doi:10.1002/eem2.12028

Kang, W., Wang, Y., and Xu, J. (2017). Recent Progress in Layered Metal Dichalcogenide Nanostructures as Electrodes for High-Performance Sodium-Ion Batteries. *J. Mater. Chem. A.* 5, 7667–7690. doi:10.1039/c7ta00003k

Lei, Y., Yang, M., Hou, J., Wang, F., Cui, E., Kong, C., et al. (2018). Thiomolybdate [Mo3S13]2−nanocluster: a Molecular Mimic of MoS2active Sites for Highly Efficient Photocatalytic Hydrogen Evolution. *Chem. Commun.* 54, 603–606. doi:10.1039/c7cc08178b

Li, D.-N., Shao, F.-Q., Feng, J.-J., Wei, J., Zhang, Q.-L., and Wang, A.-J. (2018a). Uniform Pt@Pd Nanocrystals Supported on N-Doped Reduced Graphene Oxide as Catalysts for Effective Reduction of Highly Toxic Chromium(VI). *Mater. Chem. Phys.* 205, 64–71. doi:10.1016/j.matchemphys.2017.10.074

Li, J., Wang, H., Wei, W., and Meng, L. (2018c). Advanced MoS2 and Graphene Heterostructures as High-Performance Anode for Sodium-Ion Batteries. *Nanotechnology* 30, 104003. doi:10.1088/1361-6528/aaf76c

Li, J., Han, L., Li, Y., Li, J., Zhu, G., Zhang, X., et al. (2020). MXene-Decorated SnS2/Sn3S4 Hybrid as Anode Material for High-Rate Lithium-Ion Batteries. *Chem. Eng. J.* 380, 122590. doi:10.1016/j.cej.2019.122590

Li, J., Han, L., Zhang, X., Sun, H., Liu, X., Lu, T., et al. (2021). Multi-role TiO2 Layer Coated Carbon@few-Layered MoS2 Nanotubes for Durable Lithium Storage. *Chem. Eng. J.* 406, 126873. doi:10.1016/j.cej.2020.126873

Li, J., Han, L., Zhang, X., Zhu, G., Chen, T., Lu, T., et al. (2019a). Sb2O5/Co-containing Carbon Polyhedra as Anode Material for High-Performance Lithium-Ion Batteries. *Chem. Eng. J.* 370, 800–809. doi:10.1016/j.cej.2019.03.244

Li, J., Peng, Q., Zhou, J., Sun, Z., and Sun, Z. (2019b). MoS2/Ti2CT2 (T = F, O) Heterostructures as Promising Flexible Anodes for Lithium/Sodium Ion Batteries. *J. Phys. Chem. C* 123, 11493–11499. doi:10.1021/acs.jpcc.9b01648

Li, Y., Ma, X., Ju, J., Sun, X., Deng, N., Li, Z., et al. (2018b). Preparation and Characterization of Crosslinked Electrospun Pullulan Nanofiber Membrane as a Potential for Biomaterials. *J. Textile Inst.* 109, 750–756. doi:10.1080/00405000.2017.1368107

Li, Z., Xu, Z., Tan, X., Wang, H., Holt, C. M. B., Stephenson, T., et al. (2013). Mesoporous Nitrogen-Rich Carbons Derived from Protein for Ultra-high Capacity Battery Anodes and Supercapacitors. *Energy Environ. Sci.* 6, 871–878. doi:10.1039/c2ee23599d

Liu, R.-S., and Mustarelli, P. (2020). Editorial: Electrode Materials for Lithium and Post-Lithium Rechargeable Batteries. *Front. Mater.* 7, 48. doi:10.3389/fmats.2020.00048

Liu, Y., Zhu, J., Xu, J., Liu, S., Li, L., Zhang, C., et al. (2018). High-temperature Solvent-free Sulfidation of MoO3 Confined in a Polypyrrole Shell: MoS2 Nanosheets Encapsulated in a Nitrogen, Sulfur Dual-Doped Carbon Nanoprism for Efficient Lithium Storage. *Nanoscale* 10, 7536–7543. doi:10.1039/c8nr00068a

Lv, R., Robinson, J. A., Schaak, R. E., Sun, D., Sun, Y., Mallouk, T. E., et al. (2015). Transition Metal Dichalcogenides and beyond: Synthesis, Properties, and Applications of Single- and Few-Layer Nanosheets. *Acc. Chem. Res.* 48, 56–64. doi:10.1021/ar5002846

Ma, T., Liu, X., Sun, L., Xu, Y., Zheng, L., and Zhang, J. (2019). MoS2 nanosheets@N-Carbon Microtubes: A Rational Design of Sheet-On-Tube Architecture for Enhanced Lithium Storage Performances. *Electrochimica Acta* 293, 432–438. doi:10.1016/j.electacta.2018.10.066

Nayak, P. K., Yang, L., Brehm, W., and Adelhelm, P. (2018). From Lithium-Ion to Sodium-Ion Batteries: Advantages, Challenges, and Surprises. *Angew. Chem. Int. Ed.* 57, 102–120. doi:10.1002/anie.201703772

Ni, L., Wang, R., Fu, Y., Wang, H., Liu, W., Zhu, L., et al. (2019b). Nanoengineering Mesoporous Graphene-Based Anatase/bronze TiO2 Heterostructures for Pseudocapacitance-Enhanced Lithium-Ion Batteries. *J. Alloys Compd.* 790, 683–692. doi:10.1016/j.jallcom.2019.03.237

Ni, L., Wang, R., Wang, H., Jing, W., Zhu, L., Qiu, S., et al. (2019a). Surface-induced Synthesis of Hybrid N, P Functionalized Hierarchically Porous Carbon Nanosheets for Lithium-Ion Batteries. *Microporous Mesoporous Mater.* 282, 197–204. doi:10.1016/j.micromeso.2019.03.035

Ni, L., Wang, R., Wang, H., Sun, C., Sun, B., Guo, X., et al. (2018). Designing Nanographitic Domains in N-Doped Porous Carbon Foam for High Performance Supercapacitors. *Carbon* 139, 1152–1159. doi:10.1016/j.carbon.2018.07.057

Palacín, M. R. (2009). Recent Advances in Rechargeable Battery Materials: a Chemist's Perspective. *Chem. Soc. Rev.* 38, 2565–2575. doi:10.1039/b820555h

Peng, L., Zhu, Y., Chen, D., Ruoff, R. S., and Yu, G. (2016). Two-Dimensional Materials for Beyond-Lithium-Ion Batteries. *Adv. Energ. Mater.* 6, 1600025. doi:10.1002/aenm.201600025

Pu, F., Bai, Y., Lv, J., Zhao, X., Wu, G., Kong, C., et al. (2021). Yolk-Shell Cu 2 O@CuO-decorated RGO for High-Performance Lithium-Ion Battery Anode. *Energ. Environ. Mater.*, 1–8. doi:10.1002/eem2.12160

Quinlan, R. A., Lu, Y.-C., Kwabi, D., Shao-Horn, Y., and Mansour, A. N. (2016). XPS Investigation of the Electrolyte Induced Stabilization of LiCoO2and "AlPO4"-Coated LiCoO2Composite Electrodes. *J. Electrochem. Soc.* 163, A300–A308. doi:10.1149/2.0851602jes

Sen, U. K., Johari, P., Basu, S., Nayak, C., and Mitra, S. (2014). An Experimental and Computational Study to Understand the Lithium Storage Mechanism in Molybdenum Disulfide. *Nanoscale* 6, 10243–10254. doi:10.1039/c4nr02480j

Song, W., Zhang, Y., Varyambath, A., and Kim, I. (2019). Guided Assembly of Well-Defined Hierarchical Nanoporous Polymers by Lewis Acid-Base Interactions. *ACS Nano* 13 (10), 11753–11769. doi:10.1021/acsnano.9b05727

Song, W., Zhang, Y., Varyambath, A., Kim, J. S., and Kim, I. (2020b). Sulfonic Acid Modified Hollow Polymer Nanospheres with Tunable wall-thickness for Improving Biodiesel Synthesis Efficiency. *Green. Chem.* 22, 3572–3583. doi:10.1039/d0gc00905a

Song, W., Zhang, Y., Yu, D.-G., Tran, C. H., Wang, M., Varyambath, A., et al. (2020a). Efficient Synthesis of Folate-Conjugated Hollow Polymeric Capsules for Accurate Drug Delivery to Cancer Cells. *Biomacromolecules* 22 (2), 732–742. doi:10.1021/acs.biomac.0c01520

Tarascon, J.-M., and Armand, M. (2001). Issues and Challenges Facing Rechargeable Lithium Batteries. *Nature* 414, 359–367. doi:10.1038/35104644

Wan, Z., Shao, J., Yun, J., Zheng, H., Gao, T., Shen, M., et al. (2014). Core-Shell Structure of Hierarchical Quasi-Hollow MoS2Microspheres Encapsulated Porous Carbon as Stable Anode for Li-Ion Batteries. *Small* 10, 4975–4981. doi:10.1002/smll.201401286

Wang, J., Luo, C., Gao, T., Langrock, A., Mignerey, A. C., and Wang, C. (2015). An Advanced MoS2/Carbon Anode for High-Performance Sodium-Ion Batteries. *Small* 11, 473–481. doi:10.1002/smll.201401521

Wang, X., Shen, X., Wang, Z., Yu, R., and Chen, L. (2014). Atomic-Scale Clarification of Structural Transition of MoS2upon Sodium Intercalation. *ACS Nano* 8, 11394–11400. doi:10.1021/nn505501v

Wu, J., Lu, Z., Li, K., Cui, J., Yao, S., Ihsan-ul Haq, M., et al. (2018). Hierarchical MoS2/Carbon Microspheres as Long-Life and High-Rate Anodes for Sodium-Ion Batteries. *J. Mater. Chem. A.* 6, 5668–5677. doi:10.1039/c7ta11119c

Yabuuchi, N., Kubota, K., Dahbi, M., and Komaba, S. (2014). Research Development on Sodium-Ion Batteries. *Chem. Rev.* 114, 11636–11682. doi:10.1021/cr500192f

Yan, D., Huang, S., Von Lim, Y., Fang, D., Shang, Y., Pam, M. E., et al. (2020). Stepwise Intercalation-Conversion-Intercalation Sodiation Mechanism in CuInS2 Prompting Sodium Storage Performance. *ACS Energ. Lett.* 5, 3725–3732. doi:10.1021/acsenergylett.0c02049

Yan, D., Yu, C., Bai, Y., Zhang, W., Chen, T., Hu, B., et al. (2015). Sn-doped TiO2 Nanotubes as superior Anode Materials for Sodium Ion Batteries. *Chem. Commun.* 51, 8261–8264. doi:10.1039/c4cc10020d

Yan, J. M., Huang, H. Z., Zhang, J., Liu, Z. J., and Yang, Y. (2005). A Study of Novel Anode Material CoS2 for Lithium Ion Battery. *J. Power Sourc.* 146, 264–269. doi:10.1016/j.jpowsour.2005.03.144

Ye, J., Zang, J., Tian, Z., Zheng, M., and Dong, Q. (2016). Sulfur and Nitrogen Co-doped Hollow Carbon Spheres for Sodium-Ion Batteries with superior Cyclic and Rate Performance. *J. Mater. Chem. A.* 4, 13223–13227. doi:10.1039/c6ta04592h

Yuan, C., Hou, L., Yang, L., Fan, C., Li, D., Li, J., et al. (2011). Interface-hydrothermal Synthesis of Sn3S4/graphene Sheet Composites and Their Application in Electrochemical Capacitors. *Mater. Lett.* 65, 374–377. doi:10.1016/j.matlet.2010.10.045

Yue, X.-Z., Li, C.-Q., Liu, Z.-Y., Yi, S.-S., Chen, D.-L., Wang, F., et al. (2019). Steering Charge Kinetics in W2C@C/TiO2 Heterojunction Architecture: Efficient Solar-Light-Driven Hydrogen Generation. *Appl. Catal. B: Environ.* 255, 117760. doi:10.1016/j.apcatb.2019.117760

Zhang, X., Zhao, R., Wu, Q., Li, W., Shen, C., Ni, L., et al. (2018). Ultrathin WS2 Nanosheets Vertically Embedded in a Hollow Mesoporous Carbon Framework - a Triple-Shell Structure with Enhanced Lithium Storage and

Electrocatalytic Properties. *J. Mater. Chem. A.* 6, 19004–19012. doi:10.1039/c8ta05584j

Zhao, Q., Zhai, C., Lu, Q., and Zhang, M. (2019). Effect of Ho Dopant on the Ferromagnetic Characteristics of MoS2 Nanocrystals. *Phys. Chem. Chem. Phys.* 21, 232–237. doi:10.1039/c8cp05790g

Zhou, J., Qin, J., Zhang, X., Shi, C., Liu, E., Li, J., et al. (2015). 2D Space-Confined Synthesis of Few-Layer MoS2 Anchored on Carbon Nanosheet for Lithium-Ion Battery Anode. *ACS Nano* 9, 3837–3848. doi:10.1021/nn506850e

Zhuang, W., Li, L., Zhu, J., An, R., Lu, L., Lu, X., et al. (2015). Facile Synthesis of Mesoporous MoS2-TiO2Nanofibers for Ultrastable Lithium Ion Battery Anodes. *ChemElectroChem* 2, 374–381. doi:10.1002/celc.201402358

Conflict of Interest: Authors XZ, CM, and HS are employed by Beijing Smartchip Semiconductor Technology Co., Ltd. and Beijing Smart-Chip Microelectronics Technology Co., Ltd. Authors KL, LL, HW, and XH are employed by Beijing Smart-Chip Microelectronics Technology Co., Ltd.

The remaining authors declare that the research was conducted in the absence of any commercial or financial relationships that could be construed as a potential conflict of interest.

Publisher's Note: All claims expressed in this article are solely those of the authors and do not necessarily represent those of their affiliated organizations, or those of the publisher, the editors and the reviewers. Any product that may be evaluated in this article, or claim that may be made by its manufacturer, is not guaranteed or endorsed by the publisher.